

WMCP-EM: An integrated dehazing framework for visibility restoration in single image

Sidharth Gautam*, Tapan Kumar Gandhi, B.K. Panigrahi

Indian Institute of Technology, New Delhi, India



ARTICLE INFO

Communicated by Nikos Paragios

MSC:
41A05
41A10
65D05
65D17

Keywords:
Image dehazing
Image restoration
Image enhancement

ABSTRACT

Adopting local patches for varying haze conditions is crucial for optimizing the performance in single image dehazing. We propose a novel two-fold method with a prime focus on self-adaptive prior named Weighted Median Channel Prior (WMCP) to resolve the problems introduced by using a fixed size local-patch in the dehazing process. WMCP works by leveraging the spatially changing haze statistics such as inclusion-exclusion of related pixels for estimating depth-map in varying haze conditions. It is a scale-invariant technique that retains most of the information present in the local neighbourhood of the hazy input image for estimating scene depth, which traditional methods generally fail to preserve. In addition, an unsharp-masking based technique called edge-modulation (EM) promotes hidden or missing details such as microscopic edges and textures lost due to haze, making this scheme beneficial in ensuring a visually aesthetic and realistic dehazed image. This research also includes a set of ablation tests to assess the contributions of each module engaged in the dehazing process. We performed a comparative evaluation of our method with several state-of-the-art techniques, revealing its superiority in terms of visibility improvement and edge preservation, especially when the dense haze regions are taken into consideration.

1. Introduction

Hazy or smoky environments obscure vision and cause difficulty discerning the actual colours and textures of the scene. However, these image features are the prerequisites for many vision-based automated systems and applications, such as object detection, recognition, navigation and monitoring. Haze reduces vision by scattering and absorbing the majority of light energy in the atmosphere, making it harder to gaze and understand further, resulting in a considerable reduction in the overall clarity of the captured images. Within the last decade, the problem of single image restoration has become highly demanding as most photos are now taken with a smartphone or compact cameras. Since captured scenes are usually short-lived and difficult to recreate, the growing interest in their reconstruction has made the dehazing problem a popular topic among computer vision and graphics researchers. Dehazing methods are broadly categorized into four main groups: (i) Priors-based methods, (ii) Optimization-based methods, (iii) CNN-based methods, and (iv) GANs-based methods.

Priors-based method: To remove haze effects, a significant breakthrough has been made by He et al. (2011) by introducing a statistical prior referred to as the dark channel prior (i.e., DCP). Although the DCP method is straightforward and proven to be a useful starting point for transmission-map estimation, it fails to produce satisfactory performance when any portion of the input image is covered with dense haze

or bright object. To obviate challenges faced by DCP (He et al., 2011), many dehazing algorithms (Gibson et al., 2012; Jiang et al., 2017; Singh and Kumar, 2018; Golts et al., 2020; Yang and Sun, 2018; Zhao et al., 2018, 2021) have been developed on the basic structure of DCP. Likewise, Zhu et al. (2015) introduced a machine learning approach to model the scene depth and created colour-attenuation-prior (i.e., CAP). However, any inaccuracy in the inherent prior relationship may hinder overall dehazing performance. Similarly, Bui and Kim (2018), presented colour-ellipsoid prior (i.e., CEP) and Berman et al. (2016, 2020), developed colour-line prior and Haze-line Prior for dehazing. Kim et al. (2020) use the statistical property of the saturation component for T -map estimation. Many other priors, such as Atmospheric Illumination Prior (Wang et al., 2019) and Gamma Correction Prior (Ju et al., 2020) have also been developed to accelerate dehazing research. The main issue with prior-based methods is that they are excessively vulnerable to describing the haze assumption on natural images. When the assumed accuracy of priors fails, they perform poorly by introducing unpleasant artefacts into their results (Li et al., 2017c).

Optimization-based methods: Unlike the methods mentioned above, which use different priors, Meng et al. (2013) developed a boundary constraint induced regularization scheme for dehazing. Later, Baig et al. (2016) improved (Meng et al., 2013) work using weighted regularization relying on entropy and quad-tree decomposition. Yang

* Corresponding author.

E-mail address: sidharthgautam02@gmail.com (S. Gautam).

and Sun (2018) combined traditional DCP with an iterative optimization algorithm in a deep-learning framework to benefit from recursive regularization for effective dehazing. To overcome the flaws of the classical DCP, Zhao et al. (2019a) suggested a multi-scale fusion approach, namely MOF, which combines two or more images into a single image while keeping only the important features. Recently, Kar et al. (2020) proposed LSTM driven end-to-end dehazing network for jointly optimizing the air-light and transmission-map. Wu et al. (2020) devised a semantic-guided optimization scheme to smooth out the abrupt transition to improve the accuracy of transmission-map. Similarly, Lu et al. (2020) proposed a saturation-based iterative regularization approach to rectify the issue of transmission under-estimation for effective dehazing. The main issue with optimization-based solutions is that they are highly computationally intensive and take much time to update the intermediate stage parameters.

CNN-based methods: Over the past few years, substantial progress has been made to solve the dehazing problem by exploring image-level information and hierarchical features using deep-learning frameworks (Tang et al., 2014; Cai et al., 2016; Ren et al., 2016; Zhang and Patel, 2018; Liu et al., 2019; Zhang et al., 2020; Li et al., 2021a), and hybrid-models (Li et al., 2017a; Yang and Sun, 2018; Du and Li, 2018; Chen et al., 2016; Li et al., 2017b; Zhao et al., 2019a; Chen et al., 2021; Zhao et al., 2021) to intelligently learn the dehazing characteristics from the input haze image via supervised learning. In deep-learning, Tang et al. (2014) used an ensemble of haze-relevant attributes to estimate the haze contribution under the random-forest framework. But, these features do not generalize well to specific situations, such as dense haze, bright objects, and sky-regions in hazy images. Inspired by Tang's work, Cai et al. (2016) developed an end-to-end trainable CNN (i.e., convolutional neural network) named dehazenet to learn the translation function for dehazing. Meanwhile, Ren et al. (2016) also proposed an MSCNN-based dehazing method. Analogously, Zhang and Patel (2018) developed DCPDN, a fully connected dehazing network. In the hybrid framework, Li et al. (2017a) developed an optimized cumulative network, named AOD-Net, to learn multiple parameters involved in the dehazing process collectively. Chen et al. (2016) developed a dehazing method using GRM (i.e., gradient residual minimization). Cho et al. (2018) used a model-assisted fusion approach, which often results in artificial and synthetic dehazing due to multi-band over-enhancement. Dhara et al. (2020) used weighted least squares filtering on DCP for elaborating image details.

In addition to the aforementioned approaches, many other techniques (Li et al., 2018; Ren et al., 2018; Das and Dutta, 2020; Dong et al., 2020; Wu et al., 2020; Chen et al., 2022) have also been developed to avoid artefact concerns. However, their dehazing efficacy is impeded by slow model convergence, unavailability of paired datasets (i.e., haze and haze-free images) for model training. Also, the data-driven methods require paired datasets (i.e., haze and haze-free images) for proper training of the CNN model, which is not readily available and needs substantial manual labour to generate. Furthermore, when the hyperparameters are suboptimal, under-fitting causes hazy residues in dehazing outcomes. The data-driven models are also prone to overfitting, where they learn the solution and the noise due to the extreme complexity of the network and not the true mappings. Conclusively, they do well on the training datasets but not on unseen data.

GANs-based methods: To overcome the problem of paired datasets, a new framework called GANs (i.e., generative adversarial networks) (Goodfellow et al., 2014) has been used by Zhang and Patel (2018), Li et al. (2018), Engin et al. (2018), Zhao et al. (2019b), Qu et al. (2019) and Dong et al. (2020) to generate realistic haze-free images without relying on the atmospheric imaging model. A densely connected pyramid dehazing network relying on GAN is investigated by Zhang and Patel (2018), where the reconstruction error between two sets of training data aimed to be minimized for subtle dehazing effects. An end-to-end conditional GAN is contributed by Li et al. (2018). Furthermore, for high-resolution dehazing results, Engin et al.

(2018) employed a laplacian-pyramid based up-sampling scheme in their cycle-dehaze network. To obviate the problem of paired data set in adversarial training, a dehazing scheme called Double-Discriminator Cycle-Consistent Adversarial Networks (i.e., DD-CycleGAN) is proposed by Zhao et al. (2019b). Likewise, a supervised dehazing framework called RefineDNet (Zhao et al., 2021) was also proposed, combining key aspects of both prior-based and data-driven approaches via adversarial learning. Zhang and Tao (2020) proposed FAMED-Net, which fused the response from a three-scale encoder for dehazing. Qu et al. (2019) presented a dehazing network called EPDN to learn image translation mappings using the visual perception theory. Similarly, Dong et al. (2020) designed a dehazing network based on GAN architecture with dense feature fusion called MSBDN for dehazing.

Aside from the methods mentioned above, several other dehazing algorithms (Deng et al., 2020; Anvari and Athitsos, 2020; Sun et al., 2021; Zhao et al., 2021; Li et al., 2021b; Wu et al., 2021; Liu et al., 2022) have demonstrated substantial progress using GANs. In these methods, retraining and fine-tuning the hyperparameters are the limiting factors when the distribution of new unseen data does not match the distribution of the trained data. Furthermore, extensive and time-consuming training requires specialized hardware with high computational capabilities (TPUs/GPUs), which are expensive and often inaccessible.

Typical GANs require much larger datasets compared to data-driven architectures such as CNNs. Covering all the haze scenarios and possibilities in a limited dataset is unreasonable, and the ill-posed nature of the dehazing problem makes it arduous to find a generalized solution. Therefore, to make it well-posed many image priors and assumptions used in the conventional dehazing frameworks have significant inconveniences as they impose hard bounding constraints for the problem's solution and may not always produce distortion-free results under varying haze conditions. To overcome such challenges, we have proposed an integrated framework for visibility restoration in a single haze images. The utility of the proposed methodology is to solve the dark channel's hard zeroing constraint without brute-forcing a highly non-convex equation. Our methodology aims to lessen the inaccuracy of the medium transmittance caused by brute-forcing hard zeroing constraints of DCP. The significant contributions of our manuscript are summarized as follows:

1. Primarily, a self-adaptive prior named weighted median channel prior (WMCP) has been proposed to address the problem of fixed-size local-patches by finding the optimal local-patches under varying haze conditions.
2. Secondly, considering the unsharp masking principle, an edge emphasizing modulation scheme is designed to repair the faint details in the reconstructed image.

The remainder section of this article is organized as: In Section 2, the atmospheric imaging model with the challenges prevalent to image dehazing is presented. Section 3 illustrates the proposed dehazing framework in detail. Section 4 sheds light on the experimental results, ablation study and comparison with some state-of-the-art competing methods. Finally, concluding remarks with the future direction of research are summarized in Section 5.

2. Problem definition and motivation

2.1. Atmospheric imaging model

The atmospheric imaging model (Narasimhan and Nayar, 2002) has been widely used to study the physical process of image degradation under the haze influence as:

$$I(\mathbf{x}) = J(\mathbf{x})e^{-\beta d(\mathbf{x})} + A_{\infty}(1 - e^{-\beta d(\mathbf{x})}) \quad (1)$$

$$T(\mathbf{x}) = e^{-\beta d(\mathbf{x})} \quad (2)$$

where I and $J \in \mathbb{R}^{M \times N \times 3}$ are the haze image and haze-free image, $\mathbf{x} = (x, y) \in \mathbb{R}^2$ is the pixel position, $A_\infty = [A_\infty^r, A_\infty^g, A_\infty^b]^\top \in \mathbb{R}^3$ is the global air-light, and $T \in \mathbb{R}^{M \times N}$ is the medium transmission-map or T -map exponentially correlated to the atmospheric attenuation coefficient ($\beta \in \mathbb{R} \mid 0 < \beta \leq n$), and $d(\mathbf{x}) \in \mathbb{R}^{M \times N}$ is the scene-depth. For simplicity, on rewriting, Eq. (1):

$$I(\mathbf{x}) = J(\mathbf{x})T(\mathbf{x}) + A_\infty(1 - T(\mathbf{x})) \quad (3)$$

In Eq. (3), the term $J(\mathbf{x})T(\mathbf{x})$ indicates the direct attenuation that actual scene radiance undergoes before reaching the camera. The term $A_\infty(1 - T(\mathbf{x}))$ in Eq. (3) is called the local air-light, which exponentially grows with the scene-depth $d(\mathbf{x})$ and influences the true colours by adding whiteness to the scene. In an ideal case, the range of $d(\mathbf{x})$ is $[0, +\infty)$, which makes the pixel values of the T -map lie within the range $0 < T(\mathbf{x}) \leq 1$.

$$I(\mathbf{x}) = J(\mathbf{x}), \quad \text{when } d(\mathbf{x}) \rightarrow 0, \quad T(\mathbf{x}) \rightarrow 1 \quad (4)$$

Similarly,

$$I(\mathbf{x}) = A_\infty, \quad \text{when } d(\mathbf{x}) \rightarrow \infty, \quad T(\mathbf{x}) \rightarrow 0 \quad (5)$$

According to Eq. (4), the image taken for shorter range objects is haze-free and corresponds to the true scene radiance $J(\mathbf{x})$. Similarly, Eq. (5) means that when a scenic object is located at a much greater distance from the camera ($e^{-\beta d(\mathbf{x})} \approx 0$), the effect of air-light (A_∞) is more potent, resulting in a hazy view. However, the ideal scenario given by Eqs. (4) and (5) are not feasible in practical situations. Therefore, to recover the scene radiance $J(\mathbf{x})$, both A_∞ and $T(\mathbf{x})$ need to be estimated independently (He et al., 2011; Zhu et al., 2015; Yang and Sun, 2018) using $I(\mathbf{x})$:

$$J(\mathbf{x}) = \frac{I(\mathbf{x}) - A_\infty}{T(\mathbf{x})} + A_\infty \quad (6)$$

The dehazing problem in Eq. (6) is considered to be under-constrained or ill-posed because several different pairs of A_∞ and $T(\mathbf{x})$ can generate the same $J(\mathbf{x})$. Therefore, to simplify the solution and to make the problem well-posed, it is necessary to rely on some constraints, assumptions and priors.

2.2. Dark channel prior

The DCP (He et al., 2011) works on a key insight that localized patches of at least one colour channel of haze-free image $J(\mathbf{x})$ have pixels with significant low intensity. Mathematically, it is defined as:

$$J^{Dark}(\mathbf{x}) = \min_{y \in \Omega(\mathbf{x})} \left(\min_{c \in \{r,g,b\}} J^c(y) \right) \quad (7)$$

where $\Omega = 15$ is an image fixed size local-patch. For $T(\mathbf{x})$ estimation, DCP (He et al., 2011) presumed that A_∞ is known and uses the normalized form of Eq. (1):

$$\frac{I(\mathbf{x})}{A_\infty} = \frac{J(\mathbf{x})\hat{T}(\mathbf{x})}{A_\infty} + 1 - \hat{T}(\mathbf{x}) \quad (8)$$

When DCP's Eq. (7) is substituted on both sides of Eq. (8):

$$\min_{\Omega} \left(\min_c \left(\frac{I^c(\mathbf{x})}{A_\infty^c} \right) \right) = \min_{\Omega} \left(\min_c \left(\frac{J^c(\mathbf{x})}{A_\infty^c} \right) \right) \hat{T}(\mathbf{x}) + 1 - \hat{T}(\mathbf{x}) \quad (9)$$

Accordingly, DCP (He et al., 2011), the dark channel of haze-free image $J(\mathbf{x}) \approx 0$:

$$\min_{\Omega} \left(\min_c \left(\frac{J^c(\mathbf{x})}{A_\infty^c} \right) \right) = 0 \quad (10)$$

After putting Eq. (10) into Eq. (9), $\hat{T}(\mathbf{x})$ is given by:

$$\hat{T}(\mathbf{x}) = 1 - w \left\{ \min_{\Omega} \left(\min_c \left(\frac{I^c(\mathbf{x})}{A_\infty^c} \right) \right) \right\} \quad (11)$$

where $w(0 < w \leq 1)$ is a constant to preserve a little haze for distant objects.

2.3. DCP limitations

Despite good performance in dehazing, DCP has the following limitations:

2.3.1. Brute-forced hard zeroing constraint

For T -map estimation in Eq. (11), the dark channel of haze-free image is forcibly reduced to zero according to the implicit underlying presumption in Eq. (10), which turns out to be vague and invalid under bright or luminous object existence in input image (Yang and Sun, 2018). Such a type of brute-forced hard zeroing constraint is responsible for causing inaccuracies in T -map and leads to distortions for haze-free image retrieval.

2.3.2. Inefficient transmission-map estimation

Because of the use of \min operator in Eq. (11), a low intensity value indicates that the captured image is distorted with a thin or mild haze. Conversely, a high value indicates thick or dense haze. However, this is not always true. Indeed, sometimes due to the long distance between the camera and the scene, the intensity of the red colour channel decays much faster than that of the green and blue channels (Gautam et al., 2021). Therefore, a lower intensity in the red channel may mislead the DCP to perceive a thin haze layer in a dense haze situation, which is not true. Furthermore, when the intensity of any bright object in images $I(\mathbf{x})$ becomes similar to the intensity of air-light (A_∞) then, according to Eq. (11):

$$\min_{\Omega} \left(\min_c \left(\frac{I^c(\mathbf{x})}{A_\infty^c} \right) \right) \rightarrow 1 \quad \text{and} \quad \hat{T}(\mathbf{x}) \rightarrow 0 \quad (12)$$

Eq. (12) implies that DCP fails to estimate the T -map, which is the key to efficient dehazing.

3. Proposed methodology

This section presents an integrated framework of the proposed dehazing approach. The block diagram is shown in Fig. 1 and the explanation of each section is described in detail below.

3.1. Weighted median channel prior (WMCP)

A scene-depth estimation method that is based on the utilization of the weighted median operator is used in this approach. The WMCP has edge-preserving capability of the classical median filter (Gautam et al., 2018). It replaces the current pixel value with the weighted median of the neighbourhood pixels in a local-patch (Ω), contrary to conventional unweighted techniques (He et al., 2011; Gibson et al., 2012; Meng et al., 2013; Zhu et al., 2015; Cai et al., 2016; Yang and Sun, 2018) which enforces the intensity of the pixels towards minimum values. In WMCP, first, for each pixel (\mathbf{x}), the minimum value from all colour channels is chosen. Then, the median value is chosen within the local neighbourhood (Ω) after associating them with a weight function $w(\mathbf{x})$. Mathematically, it is described as (Gautam et al., 2018):

$$d(\mathbf{x}_i) = \text{med}_{y \in \Omega_i(\mathbf{x}_i)} \left(w(\mathbf{x}_i) \times \min_{c \in \{r,g,b\}} I^c(y) \right) \quad (13)$$

where Ω corresponds to a local-patch or small region in the input image $I(\mathbf{x})$, $w(\mathbf{x})$ describes the weights between the colour vectors of the neighbouring pixels that can be obtained using:

$$w(\mathbf{x}_i) = e^{-\|I(\mathbf{x}) - I(y)\|^2 / 2\sigma^2} \quad (14)$$

where σ describe the standard deviation of the input image $I(\mathbf{x})$. Here, the weight $w(\mathbf{x})$ for each pixel is calculated in eight major compass orientation: N, NE, E, SE, S, SW, W, and NW, respectively. The advantage of choosing weights using Eq. (14) is that they are rotationally symmetric (i.e., non-biased to any particular direction) and retain most of the neighbourhood's information to smoothen out the inaccuracies while scene-depth estimation.

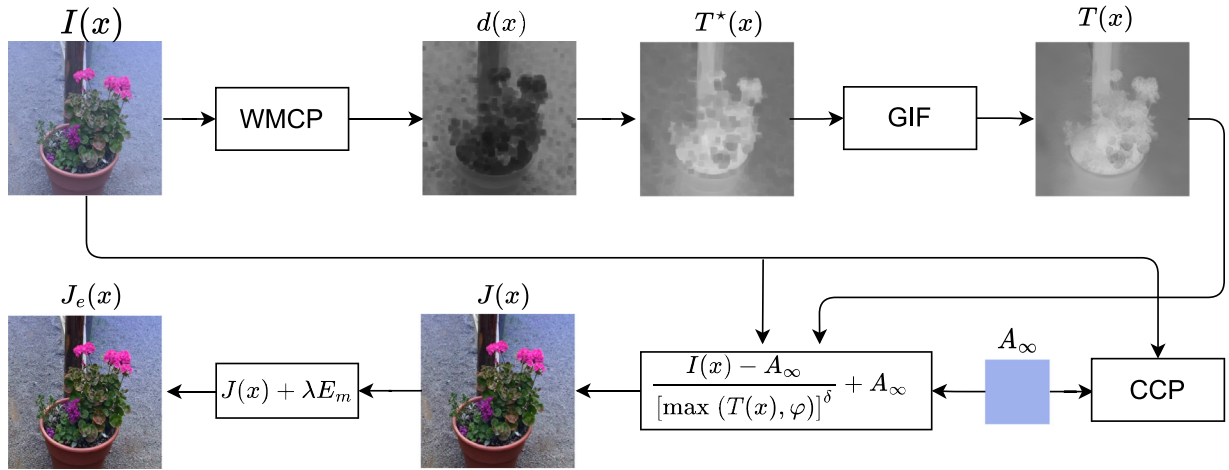
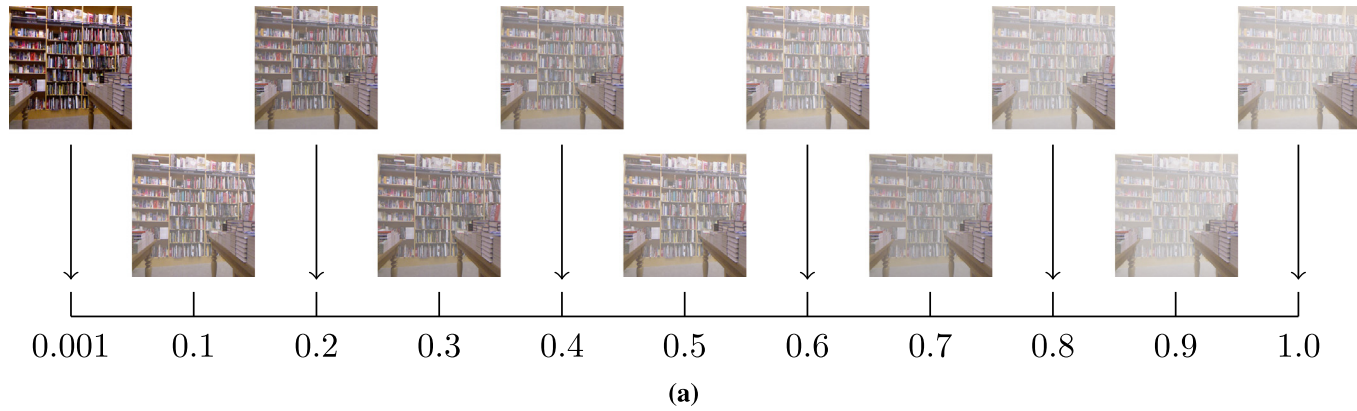
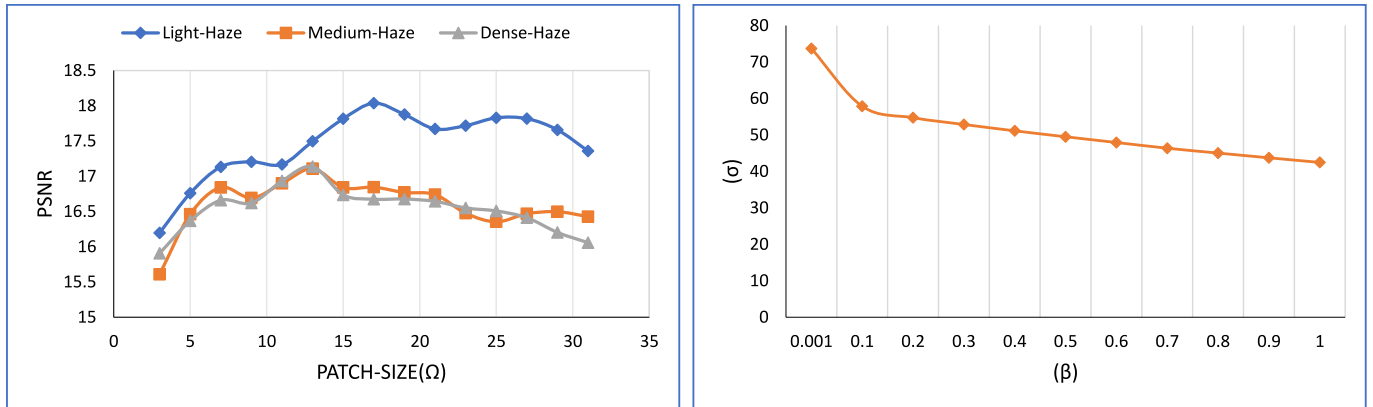


Fig. 1. The proposed integrated dehazing framework. The architecture consists of multiple stages. Firstly, the scene-depth $d(x)$ has been estimated using the proposed weighted median channel prior (WMCP), followed by T -map refinement using fast GIF (i.e. Guided Image Filter) (He and Sun, 2015). Secondly, the global air-light (A_∞) vector estimated by colour constancy prior (Gautam et al., 2020) has been used to recover the scene radiance $J(x)$. Finally, an edge emphasizing modulation technique is used to repair the faint details in $J(x)$ and to obtain the true scene radiance $J_e(x)$. (For interpretation of the references to color in this figure legend, the reader is referred to the web version of this article.)



(a)



(b)

(c)

Fig. 2. Illustration of haze statistics on RESIDE * dataset (Li et al., 2019). (a) Input images corresponding to the variable haze thickness are plotted on a β scale. (b) Average PSNR variation w.r.t. local-patch (Ω). (c) Impacts of haze density on the average standard deviation (σ). (Note: * represents manually identified 2700 images from RESIDE dataset, where haze-images corresponding to brighten scenery objects are filtered out to analyse the dehazing efficacy on the true colours of the scene in Fig. 2(b). In addition, the entire RESIDE dataset has been used in Fig. 2(c) to analyse the impacts of haze-density on the average score (σ). (For interpretation of the references to color in this figure legend, the reader is referred to the web version of this article.)

Furthermore, in Eq. (13), the patch-size (Ω) selection is critical to satisfying the assumption of constant depth in a local region of the input image (He et al., 2011; Gibson et al., 2012; Zhu et al., 2015; Tang et al., 2014; Cai et al., 2016; Fattal, 2014). Since the size of the local-patch (Ω) plays a key role in dehazing, choosing a larger (Ω) impairs

the performance by strengthening the halos artefact and delaying the run-time, whereas a smaller (Ω) make the dehazing results unnatural and over-saturated (He et al., 2011; Cai et al., 2016).

To avoid the local-patch size hurdle, a number of dehazing algorithms kept it fixed ($\Omega = 15$), irrespective of the haze statistic and



Fig. 3. Example of scene-depth $d(\mathbf{x})$ and transmission-map $T^*(\mathbf{x})$ estimation for haze image $I(\mathbf{x})$ using weighted median channel prior (WMCP). (For interpretation of the references to colour in this figure legend, the reader is referred to the web version of this article.)

image resolution. Unlike conventional dehazing algorithms (He et al., 2011; Cai et al., 2016; Galdran et al., 2017; Zhang and Patel, 2018; Yang and Sun, 2018; Wang et al., 2019; Kim et al., 2020; Ju et al., 2020), we may argue that using a fixed patch is not appropriate in the following situations: First, when the size of the local-patch (Ω) is chosen unintentionally small for images affected by light or mild haze. Second, when the local-patch (Ω) turns out to be unintentionally large for images corrupted by dense haze. We conduct a comprehensive study using a benchmark RESIDE dataset (Li et al., 2019) to investigate the haze statistics and analyse the local-patch (Ω) impacts to the dehazing robustness. Fig. 2(a) depicts haze images with variable haze thickness. Fig. 2(b) depicts the average PSNR variation w.r.t. local-patch (Ω) and Fig. 2(c) depicts the average standard deviation (σ) w.r.t. variation in haze density.

It is seen from the experimental study in Fig. 2(a) that light haze often causes the colourful appearance of scenery objects (due to the spread of pixels values over an extensive intensity range). However, selecting a small patch (Ω) in light haze makes the assumption of the constant depth in a local-region inappropriate due to the inclusion of less related pixels for depth-map estimation and severely affects the dehazing performance (see Fig. 2(b)). Similarly, under dense haze, when pixels become saturated, a large patch (Ω) selection may often limit the dehazing performance due to the inclusion of saturated pixels for depth-map estimation, resulting in the occurrence of halo-artefact around depth edges.

Fig. 2(b) presents the performance evaluations in terms of PSNR using different setting of local-patch (Ω). It can be observed from the experimental study in Fig. 2(b) that dehazing efficacy is receptive to the haze density. It is important to note that the dehazing efficacy under mild-haze conditions gradually improves with the patch-size and achieves the superior performance for ($\Omega = 17$), whereas the performance under medium and dense-haze conditions deteriorated for ($\Omega = 17$) and obtains the best PSNR score for ($\Omega = 13$). Therefore, using a fixed size of local-patch (Ω) is inappropriate, and an optimal size is needed to be calculated for robust dehazing.

The WMCP focuses on the selection of optimal patch size by taking into account the spatially changing haze-statistic of the input images, shown in Fig. 2(c). In WMCP, we try to alleviate the problem of fixed size local-patch by making it variable to the haze statistic of the input image. In WMCP, the optimal size of the local-patch (Ω) is chosen, corresponding to the pixel intensity variation in the input haze image.

Inspired by such haze statistic, the minimum possible patch size is given by:

$$\Omega = \begin{cases} \lceil \frac{\sigma}{a} \rceil + 1, & \text{if } \text{mod}(\sigma, a) = 0 \\ \lceil \frac{\sigma}{a} \rceil & \text{otherwise} \end{cases} \quad (15)$$

where σ describes the standard deviation of the input hazy image I , and a is a positive integer constant that produces an optimal local-patch (Ω). Eq. (15) implies that under the light-haze conditions, σ tends to produce higher intensity deviations due to the pixels spread over an extensive intensity range, which intermittently turns-out the size of the local-patch (Ω) to be large enough. On the contrary, under the dense-haze situation, due to the pixel's saturation σ tends to produce lower intensity deviations and, as a result, smaller size of the local-patch (Ω). From Eq. (2), it is apparent that when the scene-depth $d(\mathbf{x})$ has been estimated, the transmission-map $T^*(\mathbf{x})$ for a positive β value can be computed easily using:

$$T^*(\mathbf{x}) = e^{-\beta d(\mathbf{x})} \ominus \zeta \quad (16)$$

where \ominus is an erosion operator, and ζ represents a square structuring element. The residual of abrupt transitions in $T^*(\mathbf{x})$ is filtered out using fast GIF technique (He and Sun, 2015) (here, $*$ representing the rough estimation). Fig. 3 illustrate the estimation of $d(\mathbf{x})$ and $T^*(\mathbf{x})$ for some real haze images. Furthermore, after estimating the global air-light (A_∞) using colour constancy prior (CCP) (Gautam et al., 2020), the haze-free image $J(\mathbf{x})$ can be obtained by re-structuring Eq. (6) as:

$$J(\mathbf{x}) = \frac{I(\mathbf{x}) - A_\infty}{[\max\{T(\mathbf{x}), \varphi\}]^\delta} + A_\infty \quad (17)$$

where φ is a small positive value to avoid the problem of computational instability (i.e., division by zero), and δ is an exponent parameter for the fine detailing of dehazing effects. An example of dehazing for some real haze images is shown in Fig. 5. The proposed methodology addresses DCP's shortcomings in the following ways.

1. The proposed WMCP does not impose a brute-force hard zeroing constraint like Eq. (10) for the estimation of the T-map. As a result, WMCP is independent of introducing distortions for haze-free image retrieval, which generally appears when the underlying presumption fails when bright or luminous objects exist in the haze image.
2. In WMCP, Eq. (16) for the estimation of the T-map is independent of the condition stated under Eq. (12), thereby avoiding the erroneous estimation of T-map, which usually arises when

- the intensity of any luminous object in the input image $I(x)$ approaches the haze or air-light intensity (A_∞).
3. Furthermore, to overcome challenge's such as the low intensity of the red colour spectrum, and the under-estimation of haze density in dense haze situations, the proposed WMCP utilizes the median filter, which classical DCP fails to do.

3.2. Edge modulation

Since the true scene-radiance $J(x)$ is not as bright as the air-light (A_∞), the reconstructed image after haze-removal generally appears dim and shows faint colours and textures. For perceptual detailing, γ -correction and saturation-correction have already been suggested by He et al. (2011), Gibson et al. (2012), Berman et al. (2016), Meng et al. (2013) and Ju et al. (2019). Similarly, a technique based on histogram-stretching was presented by Tripathi and Mukhopadhyay (2012) to boost local contrast. Likewise, an optimized contrast boosting approach for dehazing was introduced by Kapoor et al. (2019), Kim et al. (2013), Cho et al. (2018) and Ju et al. (2021). There are other approaches like Retinex theory (Galdran et al., 2017) and wavelet (He et al., 2019; Liu et al., 2017) to improve the dynamic range. Due to significant variation in image contents, an optimum value of γ is difficult to be found, while the histogram-based approach overshoots the high-contrast areas and results in unpleasant artefacts.

Thus, to overcome the above constraints, the principle of unsharp masking (Gonzalez and Woods, 1992) has been explored for the development of a novel edge-modulation technique. The main objective of edge-modulated unsharp masking is to preserve the natural appearance by boosting the hidden details up to a reasonable scale. To perform edge-modulated unsharp masking, first, we calculate the luminosity $l(x)$ of the dehazed image $J(x)$ by using:

$$l(x) = \sum_c \Phi^c \times J^c(x), \quad \Phi^c = \frac{J_\mu^c}{\sum J_\mu^c} \quad (18)$$

where Φ^c are the weight contributions to each colour channel in J . Then we use a high-pass kernel (κ) to extract the edges from the image luminosity by using:

$$E = l(x) \otimes \kappa, \quad \kappa = \begin{bmatrix} -1 & -1 & -1 \\ -1 & 8 & -1 \\ -1 & -1 & -1 \end{bmatrix} \quad (19)$$

Extracted edges are then passed through the modulation function by using the following equation:

$$E_m \leftarrow E \times (Y - |l(x) - Y|) \quad (20)$$

where, Y is the edge modulation index. For instance, when $l(x)$ is near the extreme ends of the range [0, 1], the corresponding edge magnitude is reduced towards zero and thus prevents the problem of over-saturation. The modulated edges are further scaled and superimposed onto the dehazed image to obtain the true haze-free radiance by using the following transfer function:

$$J_e(x) = J(x) + \lambda E_m \quad (21)$$

where λ ($0 < \lambda \leq 1$) defines unsharp masking and gives control over the proportion of modulated edges that influence the final result. Choosing $\lambda > 1$ and large enough produces objectionable effects and a halo around the edges. The transfer function in Eq. (21) is referred to as edge modulated unsharp masking. A schematic diagram to illustrate the effects of the intermediate operations involved in edge-modulation is shown in Fig. 4. Furthermore, an impact of the edge modulated unsharp masking is shown in Fig. 5. As illustrated in Fig. 5(c), the proposed modulation approach does not employ any kind of colour or saturation correction and contrast boosting to the dehazed images shown in Fig. 5(b). By using this simple strategy, we can preserve the natural appearance while retaining even very tiny details (see Fig. 4).

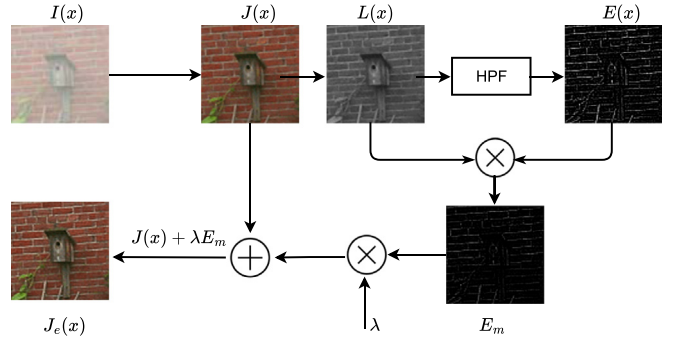


Fig. 4. Schematic figure to show the effects of various operations in the edge-modulation module.

4. Experimental results

In this section, the performance of the proposed method is evaluated against some state-of-the-art dehazing methods by conducting mass experiments on both synthetic as well as on real haze images. The haze images for experimental evaluation are obtained from the previous works, RESIDE dataset (Li et al., 2019), NTIRE dataset (Ancuti et al., 2018), and FRIDA dataset (Li et al., 2019).

4.1. Hyperparameter setting

The proposed methodology includes only a few hyperparameters. To investigate them, we conducted a series of experiments. First, we examine the significance of local-patch (Ω) selection in evaluating the dehazing efficacy. It can be seen in Fig. 2(b) that under the medium or dense-haze condition, the performance gradually drops comparatively to the light-haze condition as Ω increases. Therefore, contrary to employing a fixed parameter (i.e., $\Omega = 15$), spatially varying haze-statistic has been used to make Ω adaptive. However, for the preliminary analysis of ζ and β hyperparameters, a series of experiments have been performed on a 200+ natural haze images. The hyperparameters ζ and β has been varied from [11–21] with the step size of 2, and [0.8, 2.2] with a step size of 0.1, respectively. Based in the empirical evaluation of the above experiment, we set the value of ζ to 13, and β to 1.8. Furthermore, from experimentation selecting constants as $\gamma = 0.005$, $\varphi = 0.001$, $\delta = 0.65$, $\lambda = 0.25$, $Y = 0.5$ produced optimal results. For Fair comparison with other competing methods, we have used the code provided by the authors in their default setting to generate the dehazing results.

4.2. Evaluation on real datasets

For visual evaluation, real haze images that cover significant haze levels are selected from the dataset, as shown in Figs. 6(a)–7(a). The restored scene-radiance $J(x)$ along with other dehazing parameters (i.e., $T(x)$ and A_∞) estimated by competing algorithms (He et al., 2011; Cai et al., 2016; Li et al., 2017a; Qu et al., 2019; Zhao et al., 2019a; Kim et al., 2020; Dong et al., 2020; Zhao et al., 2021) and the proposed method are also presented.

To clearly see the dehazing effect, the reader is encouraged to zoom into the highlighted areas in Figs. 6–7. Upon zooming, one can observe multiple types of artefacts in a certain portion of the results. It can be seen from the results shown in Figs. 6–7 that all competing methods except (Li et al., 2017a; Qu et al., 2019; Dong et al., 2020) produces perceptually reasonable T -map. However, the T -map estimated by the proposed method tends to be detailed and smoothed due to the weights employed in the depth estimation process. Upon zooming, it can be observed that a large amount of blurriness exist in the T -map estimated

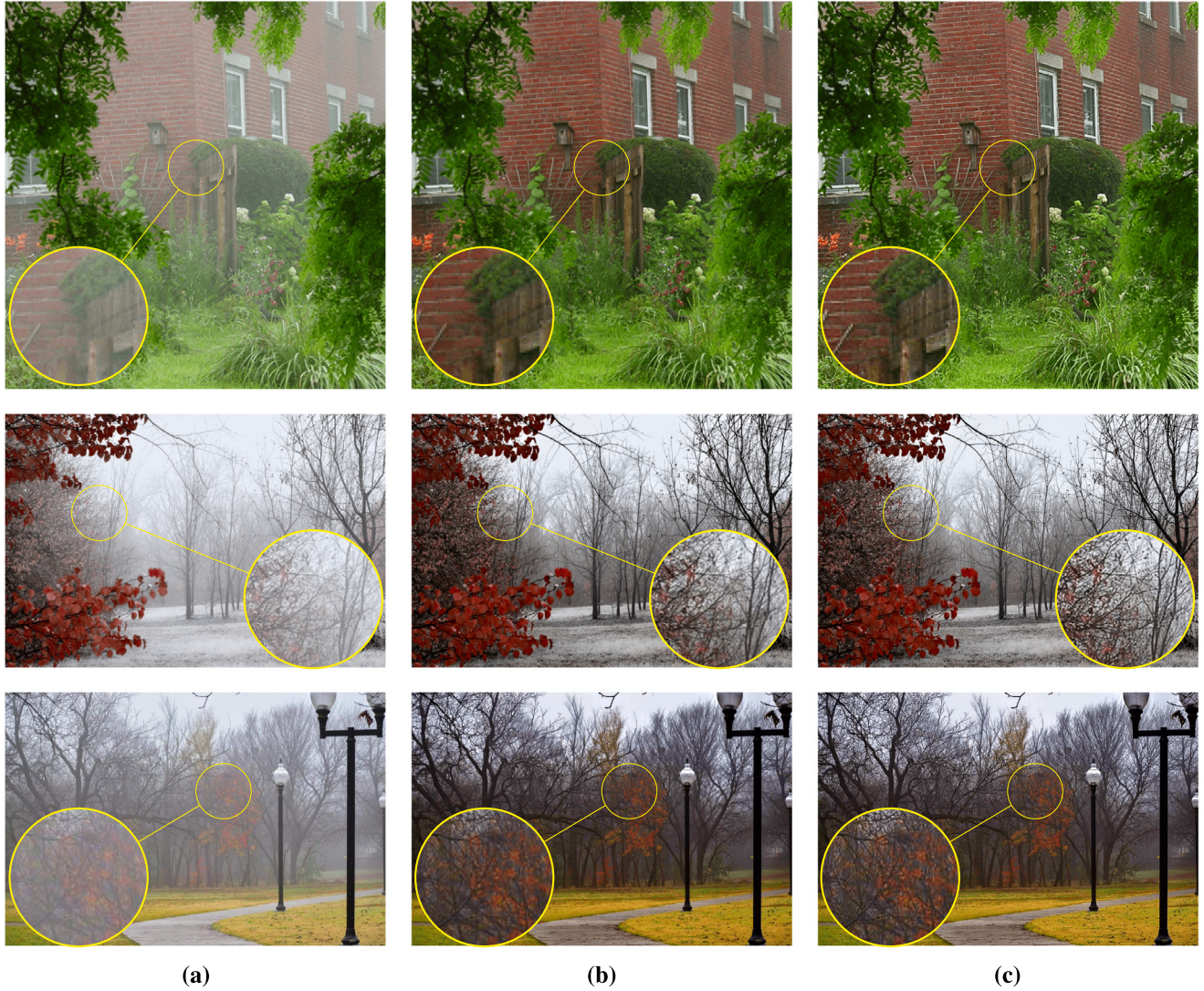


Fig. 5. Impact of edge modulated unsharp masking to the dehazing results. (a) Real haze images $J(x)$. (b) Dehazed image $J(x)$. (c) Restored scene-radiance $J_e(x)$. (Best viewed with zoom-in). (For interpretation of the references to colour in this figure legend, the reader is referred to the web version of this article.)

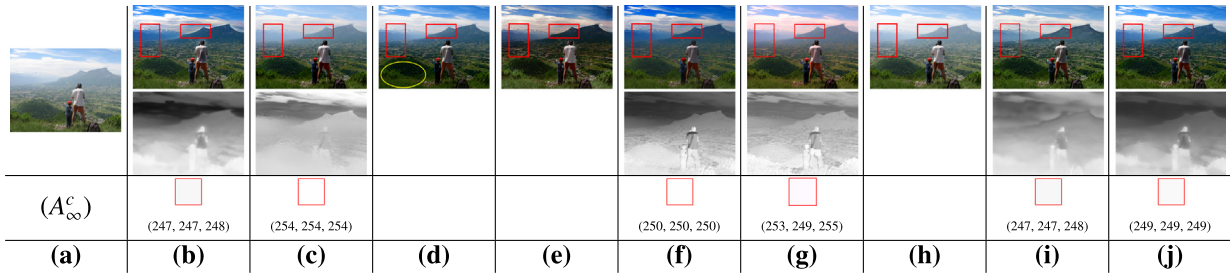


Fig. 6. Qualitative comparison of dehazing results with many other progressive techniques. (a) Real haze Image. The scene-radiance, corresponding transmission-map and air-light obtained by (b) He et al. (2011) (c) Cai et al. (2016) (d) Li et al. (2017a) (e) Qu et al. (2019) (f) Zhao et al. (2019a) (g) Kim et al. (2020) (h) Dong et al. (2020) (i) Zhao et al. (2021) (j) Ours. (Note: Li et al. (2017a) re-formulated Eq. (1) to avoid T -map estimation by integrating A_∞ and T into one parameter. Qu et al. (2019) and Zhao et al. (2021) uses a GANs architecture to learn image translation mapping for dehazing without estimating A_∞ and T -map). (For interpretation of the references to colour in this figure legend, the reader is referred to the web version of this article.)

by He et al. (2011) works, which leads to the presence of artefacts in the results.

On contrary, learning-based methods (Cai et al., 2016; Li et al., 2017a; Zhao et al., 2021) minimize the artefacts by producing over-smoothed T -map due to which recovered image $J(x)$ still appears hazy and blurry (i.e., notice the distance haze regions). It is easy to notice that Kim et al. (2020) methodology, introduces colour-shifting,

making dehazing outcomes hideous and unnatural (see Figs. 6(g)–7(g)). Conversely, Li et al. (2017a) re-formulated Eq. (1) by integrating A_∞ and T into one parameter and avoided T -map estimation. Although the approach is extremely fast, but it produces over-smoothed results and fails to yield haze-free outcomes as evenly distributed thin haze-residues can be easily seen across the dehazed results, which may arise

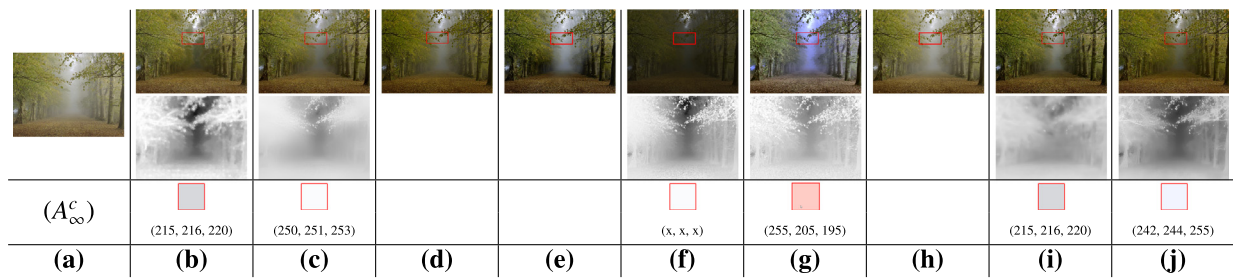


Fig. 7. Qualitative comparison of dehazing results with many other progressive techniques. (a) Real haze Image. The scene-radiance, corresponding transmission-map and air-light obtained by (b) He et al. (2011) (c) Cai et al. (2016) (d) Li et al. (2017a) (e) Qu et al. (2019) (f) Zhao et al. (2019a) (g) Kim et al. (2020) (h) Dong et al. (2020) (i) Zhao et al. (2021) (j) Ours. (Note: Li et al. (2017a) reformulated Eq. (1) to avoid T -map estimation by integrating A_∞ and T into one parameter. Qu et al. (2019) and Zhao et al. (2021) uses a GANs architecture to learn image translation mapping for dehazing without estimating A_∞ and T -map). (For interpretation of the references to colour in this figure legend, the reader is referred to the web version of this article.)

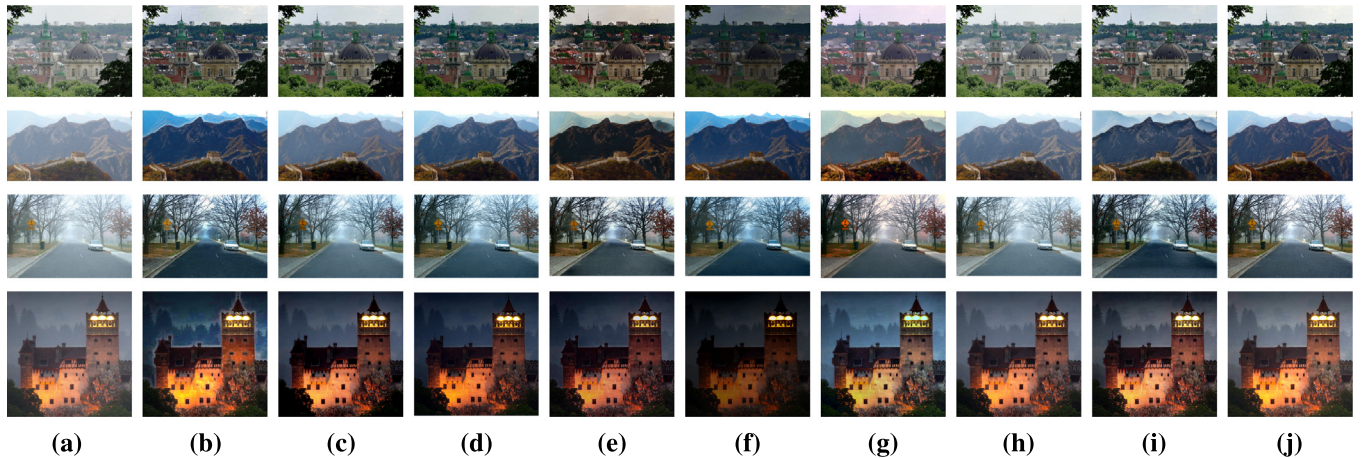


Fig. 8. Qualitative comparison of dehazing results with many other progressive techniques. (a) Real haze Image with scenery objects brighter than the air-light (A_∞). The scene-radiance obtained by (b) He et al. (2011) (c) Cai et al. (2016) (d) Li et al. (2017a) (e) Qu et al. (2019) (f) Zhao et al. (2019a) (g) Kim et al. (2020) (h) Dong et al. (2020) (i) Zhao et al. (2021) (j) Ours. (Best viewed with zoom-in).

owing to imperfect parameter learning (i.e., see the nearby bushes and tree leaves highlighted by yellow ellipse in Fig. 6(d)).

Furthermore, Qu et al. (2019) and Dong et al. (2020) utilize GANs architecture to learn the image translation mappings for dehazing without relying on the atmospheric imaging model for their parameter estimation. However, it can be evidenced in Figs. 6–7 that they are struggling to produce truly haze-free results and their result significantly suffer from over-saturation and artefact.

It can be seen in Figs. 6(j)–7(j) with properly estimated $T(x)$ and A_∞ , the proposed method generates a considerable detailed result. A qualitative comparison of dehazing results on a few challenging haze images is also shown in Fig. 8, where scenery object brighter than the haze or air-light (A_∞) exist.

4.3. Evaluation on synthetic datasets

To perform a dehazing evaluation, experiments have been carried out on three widely used synthetic haze datasets: RESIDE (Li et al., 2019), NTIRE (Ancuti et al., 2020), and FRIDA (Li et al., 2019), which provides a haze-free version of the input image as a reference. The RESIDE dataset has both indoor and outdoor images with a uniformly distributed haze over the real-world photos. However, images with variable haze densities are provided only for the indoor setting. FRIDA is a challenging dataset consisting of non-uniformly distributed dense haze over artificially generated images coupled with the luminous sky. NTIRE is a recently introduced non-uniformly distributed haze dataset to mimic real-world hazy conditions.

Figs. 9–12 shows the dehazing results of the proposed method with other approaches. For better dehazing analysis, we show the zoomed-in

regions of the hazy input, dehazed output and the reference image in Figs. Figs. 9–12, respectively. The dehazing results in Figs. Figs. 9(b)–12(b) shows that He et al. (2011) DCP approach is unable to handle white or bright objects in the input image and provides distorted outcomes when the intensity of any luminous object approaches the intensity of haze or air-light. It can be verified from the highlighted regions in Fig. 9(b) that bright objects such as ‘white papers’ tend to introduce colour distortion and boundary artefacts in the RESIDE-indoor dataset. In contrast, the results in Fig. 10(b) on the RESIDE-outdoor dataset significantly suffer from darkness than the ground truth image. Similarly, in Fig. 11(b) on the NTIRE dataset, He et al. (2011) method tends to introduce a colour-artefact (i.e., the strip of the tent house has turned from white to slight yellow). Moreover, the method fails to bring out the hidden details under heterogeneous haze conditions and is likely to introduce a colour shift in the FRIDA dataset in Fig. 12(b) (i.e., the colour tone of the sky turns out to be dark).

It can be observed that Cai et al. (2016) and Li et al. (2017a) deep-learning based techniques were successful in avoiding boundary-artefact and colour-distortion problems. However, closer inspection of their dehazing outcomes in Figs. 9(c–d)–12(c–d) reveals that both procedures struggle to obtain clean images, as substantial haze remnants are always present in their results. Qu et al. (2019) GANs-based approach succeeded in tackling the uniform haze condition in Figs. 9(e)–10(e) and produces detailed result. However, under heterogeneous haze conditions in Figs. 11(e)–12(e) it can be seen that the method fails to produce detailed results and tends to introduce colour-shifting and under-exposure problems. Similarly, Zhao et al. (2019a) approach perform well under uniform haze condition in Figs. 9(f)–10(f) but delivers underexposed findings in heterogeneous haze conditions

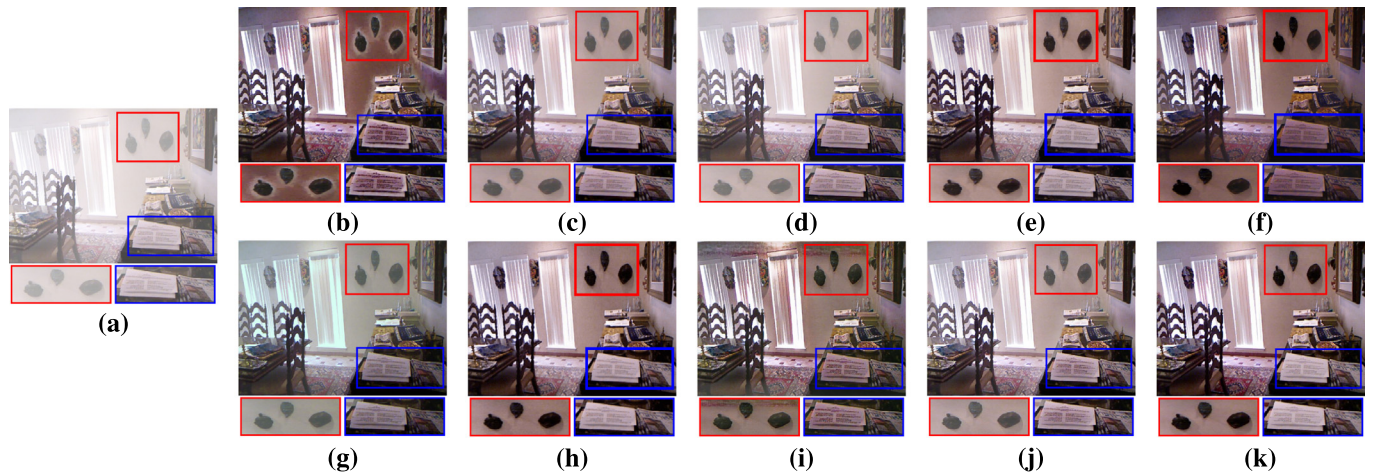


Fig. 9. Qualitative comparison of dehazing results with many other progressive techniques on RESIDE SOTS-Indoor dataset (Li et al., 2019). (a) Synthetic haze image. (b) He et al. (2011) (c) Cai et al. (2016) (d) Li et al. (2017a) (e) Qu et al. (2019) (f) Zhao et al. (2019a) (g) Kim et al. (2020) (h) Dong et al. (2020) (i) Zhao et al. (2021) (j) Ours (k) GT. (Best viewed with zoom-in). (For interpretation of the references to colour in this figure legend, the reader is referred to the web version of this article.)

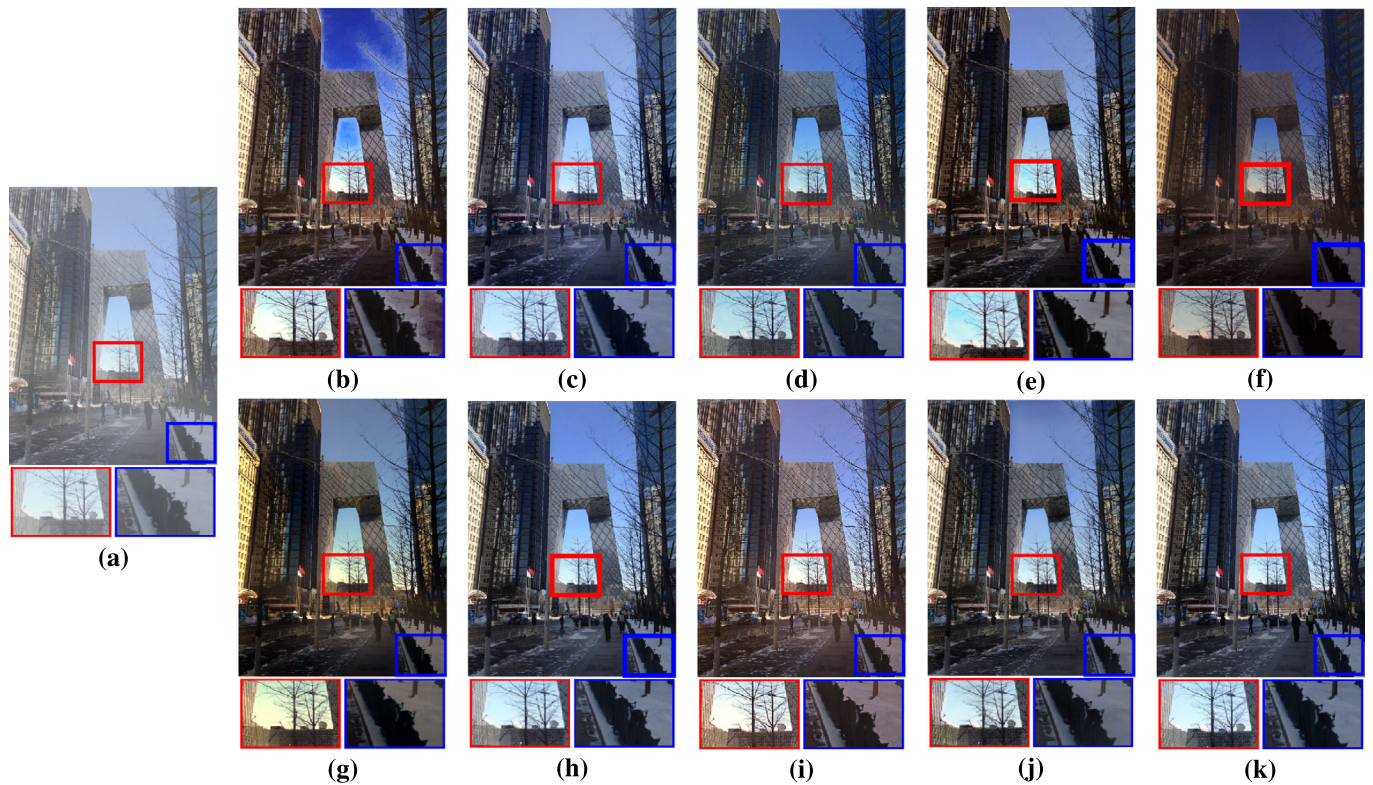


Fig. 10. Qualitative comparison of dehazing results with many other progressive techniques on RESIDE SOTS-Outdoor dataset (Li et al., 2019). (a) Synthetic haze image. (b) He et al. (2011) (c) Cai et al. (2016) (d) Li et al. (2017a) (e) Qu et al. (2019) (f) Zhao et al. (2019a) (g) Kim et al. (2020) (h) Dong et al. (2020) (i) Zhao et al. (2021) (j) Ours (k) GT. (Best viewed with zoom-in). (For interpretation of the references to colour in this figure legend, the reader is referred to the web version of this article.)

in Figs. 11(f)–12(f). It can be evidenced in Figs. 9(g)–12(g) that Kim et al. (2020) methodology, removes haze at the price of unwanted colour-shifting resulting in unsightly and disruptive outcomes (notice the colour of window curtains in Fig. 9(g) and tent strips in Fig. 12(g)). Dong et al. (2020) result in Figs. 9(h)–12(h) are aesthetically appealing, with no under-exposure. However, significant haze remnants can be seen across all dehazing outcomes under heterogeneous haze conditions in Figs. 11(h)–12(h).

The results of Zhao et al. (2021), on the other hand, are slightly better due to the absence of haze residues, but have become ineffective due to under-exposure, texture loss and artefacts issues (for instance, upon zooming Fig. 9(i), one can observe that window curtains has

changed to an unduly darker colour and spurious glitch artefacts have occurred just above the window wall). Similarly, the loss of texture and colour features can be seen in other highlighted areas of Figs. 10(i)–12(i) (i.e., a tint of yellowness in the snow, lost edge detail around the complex tent boundaries, car tail light, and the over-smoothed tree trunk), indicating that the method is adversely affected by the imprecise transmittance problem caused by the DCP brute-forced hard zeroing constraint. In contrast, the proposed method preserves the global consistency and final results shown in Figs. 9(j)–12(j) looks natural, detailed and realistic (i.e., the highlighted region seems to be clearer among the compared results).

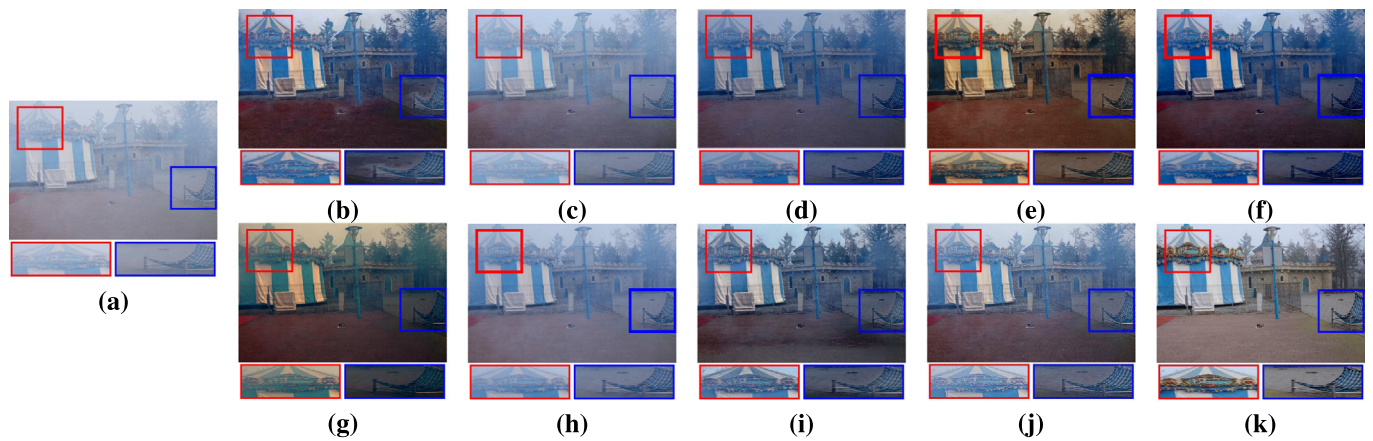


Fig. 11. Qualitative comparison of dehazing results with many other progressive techniques on NTIRE dataset (Ancuti et al., 2020). (a) Synthetic haze image. (b) He et al. (2011) (c) Cai et al. (2016) (d) Li et al. (2017a) (e) Qu et al. (2019) (f) Zhao et al. (2019a) (g) Kim et al. (2020) (h) Dong et al. (2020) (i) Zhao et al. (2021) (j) Ours (k) GT. (Best viewed with zoom-in). (For interpretation of the references to colour in this figure legend, the reader is referred to the web version of this article.)

Table 1

Quantitative comparison on synthetic RESIDE SOTS-I data-set with varying haze level.

β	Metrics	He et al. (2011)	Cai et al. (2016)	Li et al. (2017a)	Qu et al. (2019)	Zhao et al. (2019a)	Kim et al. (2020)	Dong et al. (2020)	Zhao et al. (2021)	PM
$\beta = [0.2, 0.7]$	PSNR	19.24	22.24	18.84	23.61	20.13	16.41	18.86	18.95	22.24
	SSIM	0.85	0.86	0.79	0.87	0.85	0.78	0.82	0.79	0.87
$\beta = [0.8, 1.3]$	PSNR	17.40	18.05	16.23	19.32	18.68	13.57	17.57	16.26	19.25
	SSIM	0.81	0.84	0.75	0.84	0.81	0.70	0.78	0.72	0.84
$\beta = [1.4, 1.8]$	PSNR	16.77	17.65	13.93	18.57	17.02	11.47	18.04	13.73	17.92
	SSIM	0.78	0.75	0.68	0.81	0.79	0.64	0.81	0.71	0.81

Table 2

Quantitative comparison on synthetic outdoor haze data-set with fixed haze level.

Data-Set	Metrics	He et al. (2011)	Cai et al. (2016)	Li et al. (2017a)	Qu et al. (2019)	Zhao et al. (2019a)	Kim et al. (2020)	Dong et al. (2020)	Zhao et al. (2021)	PM
RESIDE SOTS-O (Li et al., 2019)	PSNR	18.18	20.80	18.29	20.11	14.70	17.01	22.25	18.13	21.39
	SSIM	0.77	0.86	0.82	0.83	0.70	0.79	0.92	0.81	0.83
NTIRE-O (Ancuti et al., 2020)	PSNR	15.03	14.73	16.73	15.44	12.70	14.92	15.94	14.63	16.24
	SSIM	0.44	0.37	0.44	0.51	0.33	0.33	0.37	0.34	0.49
FRIDA (Tarel et al., 2012)	PSNR	11.57	11.89	12.42	11.88	10.23	12.36	11.97	11.54	12.62
	SSIM	0.62	0.62	0.71	0.53	0.51	0.62	0.71	0.70	0.71

4.4. Quantitative evaluation

To quantitatively measure of dehazing results, three quality assessment metrics, namely, peak signal-to-noise ratio (PSNR) (Ponomarenko et al., 2007), structural similarity index measurement (SSIM) (Zhang et al., 2011), and visible edges difference (E_d) (Hautière et al., 2011) has been used. Since the haze tends to wash out the image feature, the dehazing efficacy can be characterized by having less image distortion, higher structure similarity, and minimum visible edge difference.

Table 1 lists the average score of dehazing results on RESIDE SOTS-I dataset. In Table 1, three sets of indoor haze images (i.e., mild, moderate, and dense haze) are synthesized using the reference images. In Table 1, the last row corresponding to the dehazing of thick haze images shown in Fig. 9. It can be observed from Table 1 that the lowest score signifies the presence of severe haze residuals and depicts the performance of the haze-removal algorithm indirectly. For Kim et al. (2020), the average values of PSNR and SSIM are substantially lower than others, implying poor dehazing performance since the method fails to remove haze remnants and cause severe colour-shifting. Additionally, it can be seen that, Qu et al. (2019) GANs-based approach performs pretty well in indoor haze dataset and dehazed images with less distortion, and more structure similarity. However, for the outdoor haze, their results become less consistent, and fail to produce vibrant

and sparkling details. In contrast, our proposed method gives competitive performance to Qu et al. (2019) and achieves remarkable scores on the indoor dataset with mild to dense haze.

Table 2 shows the average score on three different outdoor haze datasets, namely RESIDE SOTS-O, NTIRE-O, and FRIDA. It can be evident from Table 2 that for outdoor haze datasets, the results of deep-learning based techniques (Cai et al., 2016; Qu et al., 2019; Dong et al., 2020) become less consistent as there remains a thin layer of haze residual in their result. One of the main reasons for their inconsistent performance is that all learning-based techniques perform well on the training datasets but not on unseen test images. The proposed method outperforms competitors on outdoor homogeneous and heterogeneous haze datasets, and dehazed images with less distortion, and more structure similarity.

Furthermore, the visible edges difference (E_d) shown in Fig. 13 is independent of structural similarity. It is well known that haze severely affects the visibility and thus the number of visible edges. Therefore, using the visible edges score to judge the dehazing quality is reasonable. But, the number of visible edges may often mislead, especially when boundary artefacts and distortion exist. To handle such false edge situations, the visible edge difference (E_d) between the reference image and the dehazed image can be used to generate the overall image quality. A lower score of E_d signifies that most of the microscopic details in the reference image have been restored correctly

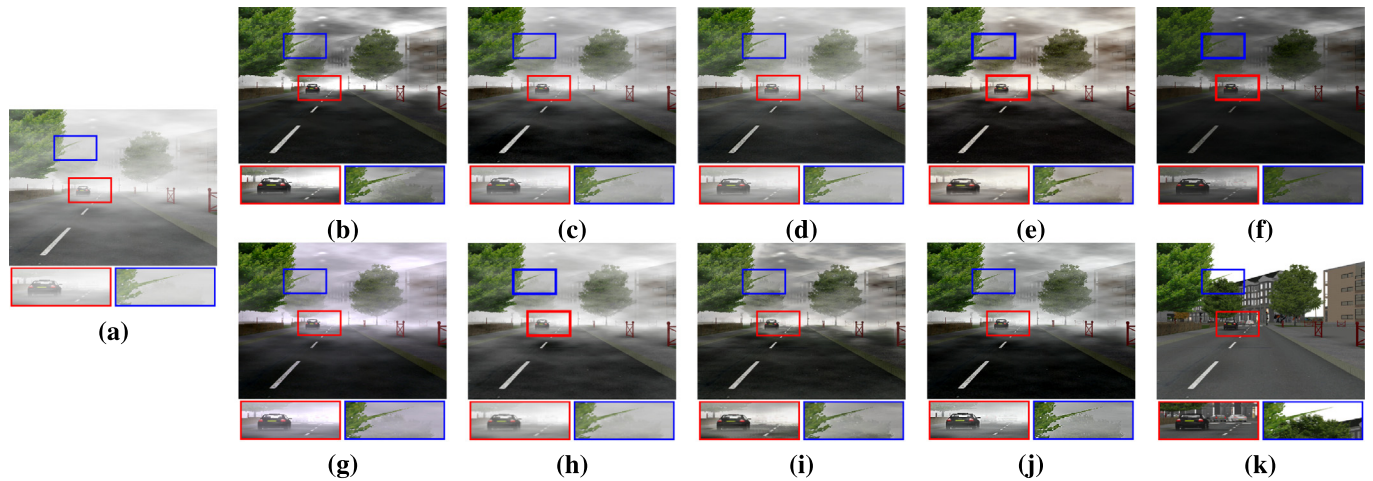


Fig. 12. Qualitative comparison of dehazing results with many other progressive techniques on FRIDA dataset (Tarel et al., 2012). (a) Synthetic haze image. (b) He et al. (2011) (c) Cai et al. (2016) (d) Li et al. (2017a) (e) Qu et al. (2019) (f) Zhao et al. (2019a) (g) Kim et al. (2020) (h) Dong et al. (2020) (i) Zhao et al. (2021) (j) Ours (k) GT. (Best viewed with zoom-in). (For interpretation of the references to colour in this figure legend, the reader is referred to the web version of this article.)

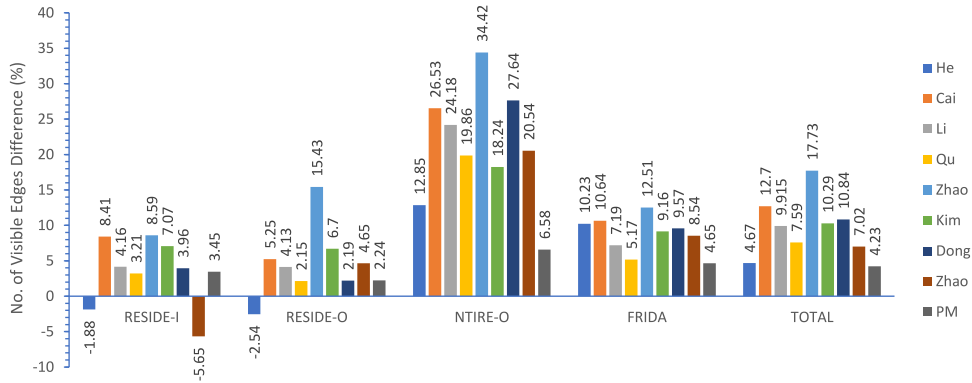


Fig. 13. Quantitative comparison of visible edge difference (E_d) with other state-of-the-art methods.

Table 3

Quantitative performance of the ablation experiments evaluated on synthetic data-set.

Parameter	Case-1	Case-2	Case-3	Case-4	Case-5	Case-6
WMCP	✓	✗	✓	✓	✓	✓
GIF	✓	✓	✗	✓	✓	✓
CCP	✓	✓	✓	✗	✓	✓
Colour exponent (δ)	✓	✓	✓	✓	✗	✓
Edge modulation (E_m)	✓	✓	✓	✓	✓	✗
RESIDE SOTS-O (Li et al., 2019)						
PSNR	21.39	19.65	12.97	20.26	19.71	21.17
SSIM	0.83	0.78	0.39	0.75	0.74	0.81

in the dehazed image, while a higher value represents poor dehazing performance and inability to recover the faint features. In contrast, a negative score indicates the presence of severe boundary artefacts in the reconstructed image.

Fig. 13 shows that the average value of E_d for (He et al., 2011) is negative due to the presence of serious boundary-artefacts. In contrast, Cai et al. (2016) and Zhao et al. (2019a) methodology consistently score the highest value of E_d , implying that the existence of haze residual in dehazed results reduces visibility and resulting in poor edge detection. The proposed method outperforms the competing methods by consistently achieving a positive minimum value of E_d for all datasets, producing aesthetically appealing and detailed dehazed results.

4.5. Ablation study

To evaluate the contributions of the different modules and components of the proposed methodology, we conduct a series of ablation experiments under the following configurations:

- Case 1: Image dehazing using the complete framework;
- Case 2: Image dehazing by replacing the WMCP with DCP while keeping other modules unchanged;
- Case 3: Image dehazing by retaining the abrupt transitions in $T^*(x)$ (i.e., without using GIF);
- Case 4: Image dehazing by including the brightest pixel set K_b for air-light estimation in CCP (Gautam et al., 2020);
- Case 5: Image dehazing by excluding the colours exponent term δ ;
- Case 6: Image dehazing by excluding the edge modulation E_m ;

Fig. 14 displays the visual effects of these configurations on the RESIDE SOTS-O (Li et al., 2019) data-set. To clearly see the contribution of each module, the reader is urged to zoom into the highlighted areas. Table 3 lists the effectiveness of each component in several ablated versions of our method by measuring image quality using PSNR and SSIM. It can be observed from Table 3 that Case-3 has the lowest quantitative performance, which implies that filtering out the abrupt transitions in $T^*(x)$ are important to suppress the artefacts and distortion for effective dehazing. In Case-2, exclusion of weighting function $w(x)$ in the proposed WMCP changes it to DCP and introduces quite a large breakdown in the overall quantitative performance of the proposed



Fig. 14. Ablation study qualitative results on the synthetic RESIDE SOTS-Outdoor data-set (Li et al., 2019). (For interpretation of the references to colour in this figure legend, the reader is referred to the web version of this article.)

method. Likewise, the inclusion of the brightest pixel set K_b for the air-light estimation in Case-4 leads to significant performance deterioration due to the undesired darkness (see Fig. 14(e)). It can be seen in Case-5 that the exponent term φ contributes more significantly and is responsible for recovering the vibrant colours in the dehazed image. Furthermore, in Case-6, the edge modulation term enhances hidden details and introduces a noticeable contribution to the overall image quality. Conclusively, the performance of Case-1 is the finest in contrast to the later cases, which justifies the fact that each module and component are contributing something to the overall method and is useful for better dehazing results.

5. Conclusion

This research investigated the challenges present in single image dehazing and addressed the problem of sizing local-patch of traditional approaches by developing a self-adaptive prior called weighted median channel prior (WMCP). To tackle varying haze conditions, WMCP selects the optimal local-patch corresponding to the haze density in the input image. Alongside solving the problem of sizing local-patch, we significantly repaired the faint details by developing an edge modulated transfer function. Extensive experimental results on various real and synthetic datasets demonstrate that the proposed method can effectively improve faint details and outperform the competing methods, mainly when dense haze regions and brighter scenery objects are considered. We believe that this research will increase the community's interest to work on several fronts of dehazing applications, including navigation, tracking, and monitoring.

CRediT authorship contribution statement

Sidharth Gautam: Conceptualization, Methodology, Data curation, Code, Writing – original draft. **Tapan Kumar Gandhi:** Supervision, Visualization, Resources, Writing – review & editing. **B.K. Panigrahi:** Supervision, Resources, Reviewing.

Declaration of competing interest

The authors declare that they have no known competing financial interests or personal relationships that could have appeared to influence the work reported in this paper.

Data availability

Data will be made available on request.

References

- Ancuti, C.O., Ancuti, C., Timofte, R., 2020. NH-HAZE: An image dehazing benchmark with non-homogeneous hazy and haze-free images. In: Proceedings of the IEEE Conference on Computer Vision and Pattern Recognition Workshops.
- Ancuti, C.O., Ancuti, C., Timofte, R., Vleeschouwer, C.D., 2018. O-HAZE: a dehazing benchmark with real hazy and haze-free outdoor images. In: IEEE Conference on Computer Vision and Pattern Recognition, NTIRE Workshop.
- Anvari, Z., Athitsos, V., 2020. Dehaze-GLCGAN: Unpaired single image de-hazing via adversarial training. <http://dx.doi.org/10.48550/ARXIV.2008.06632>, URL: <https://arxiv.org/abs/2008.06632>.
- Baig, N., Riaz, M.M., Ghafoor, A., Siddiqui, A.M., 2016. Image dehazing using quadtree decomposition and entropy-based contextual regularization. IEEE Signal Process. Lett. 23 (6), 853–857. <http://dx.doi.org/10.1109/LSP.2016.2559805>.
- Berman, D., Treibitz, T., Avidan, S., 2016. Non-local image dehazing. In: 2016 IEEE Conference on Computer Vision and Pattern Recognition. CVPR, pp. 1674–1682. <http://dx.doi.org/10.1109/CVPR.2016.185>.
- Berman, D., Treibitz, T., Avidan, S., 2020. Single image dehazing using haze-lines. IEEE Trans. Pattern Anal. Mach. Intell. 42 (3), 720–734. <http://dx.doi.org/10.1109/TPAMI.2018.2882478>.
- Bui, T.M., Kim, W., 2018. Single image dehazing using color ellipsoid prior. IEEE Trans. Image Process. 27 (2), 999–1009. <http://dx.doi.org/10.1109/TIP.2017.2771158>.
- Cai, B., Xu, X., Jia, K., Qing, C., Tao, D., 2016. DehazeNet: An end-to-end system for single image haze removal. IEEE Trans. Image Process. 25 (11), 5187–5198. <http://dx.doi.org/10.1109/TIP.2016.2598681>.
- Chen, C., Do, M.N., Wang, J., 2016. Robust image and video dehazing with visual artifact suppression via gradient residual minimization. In: Leibe, B., Matas, J., Sebe, N., Welling, M. (Eds.), Computer Vision – ECCV 2016. Springer International Publishing, Cham, pp. 576–591.
- Chen, Z., Wang, Y., Yang, Y., Liu, D., 2021. PSD: Principled synthetic-to-real dehazing guided by physical priors. In: 2021 IEEE/CVF Conference on Computer Vision and Pattern Recognition. CVPR, pp. 7176–7185. <http://dx.doi.org/10.1109/CVPR46437.2021.00710>.
- Chen, J., Yang, G., Ding, X., Guo, Z., Wang, S., 2022. Robust detection of dehazed images via dual-stream CNNs with adaptive feature fusion. Comput. Vis. Image Underst. 217, 103357. <http://dx.doi.org/10.1016/j.cviu.2022.103357>, URL: <https://www.sciencedirect.com/science/article/pii/S1077314222000017>.
- Cho, Y., Jeong, J., Kim, A., 2018. Model-assisted multiband fusion for single image enhancement and applications to robot vision. IEEE Robot. Autom. Lett. 3 (4), 2822–2829. <http://dx.doi.org/10.1109/LRA.2018.2843127>.
- Das, S.D., Dutta, S., 2020. Fast deep multi-patch hierarchical network for nonhomogeneous image dehazing. In: 2020 IEEE/CVF Conference on Computer Vision and Pattern Recognition Workshops. CVPRW, pp. 1994–2001. <http://dx.doi.org/10.1109/CVPRW50498.2020.00249>.
- Deng, Q., Huang, Z., Tsai, C.-C., Lin, C.-W., 2020. HardGAN: A haze-aware representation distillation GAN for single image dehazing. In: Computer Vision – ECCV 2020: 16th European Conference, Glasgow, UK, August 23–28, 2020, Proceedings, Part VI. Springer-Verlag, Berlin, Heidelberg, pp. 722–738. http://dx.doi.org/10.1007/978-3-030-58539-6_43.
- Dhara, S.K., Roy, M., Sen, D., Biswas, P.K., 2020. Color cast dependent image dehazing via adaptive airlight refinement and non-linear color balancing. IEEE Trans. Circuits Syst. Video Technol. 1. <http://dx.doi.org/10.1109/TCSVT.2020.3007850>.
- Dong, H., Pan, J., Xiang, L., Hu, Z., Zhang, X., Wang, F., Yang, M.-H., 2020. Multi-scale boosted dehazing network with dense feature fusion. In: 2020 IEEE/CVF Conference on Computer Vision and Pattern Recognition. CVPR, pp. 2154–2164. <http://dx.doi.org/10.1109/CVPR42600.2020.00223>.
- Du, Y., Li, X., 2018. Recursive deep residual learning for single image dehazing. In: 2018 IEEE/CVF Conference on Computer Vision and Pattern Recognition Workshops (CVPRW). pp. 843–8437.
- Engin, D., Genç, A., Ekenel, H.K., 2018. Cycle-dehaze: Enhanced CycleGAN for single image dehazing. CoRR [abs/1805.05308](https://arxiv.org/abs/1805.05308). URL: <http://arxiv.org/abs/1805.05308>, arXiv:1805.05308.
- Fattal, R., 2014. Dehazing using color-lines. ACM Trans. Graph. 34 (1), 13:1–13:14. <http://dx.doi.org/10.1145/2651362>, URL: <http://doi.acm.org/10.1145/2651362>.
- Galdran, A., Alvarez-Gil, A., Bria, A., Vazquez-Corral, J., Bertalmio, M., 2017. On the duality between retinex and image dehazing. CoRR [abs/1712.02754](https://arxiv.org/abs/1712.02754), arXiv:1712.02754.
- Gautam, S., Gandhi, T.K., Panigrahi, B.K., 2018. An advanced visibility restoration technique for underwater images. In: 2018 25th IEEE International Conference on Image Processing. ICIP, pp. 1757–1761. <http://dx.doi.org/10.1109/ICIP.2018.8451248>.
- Gautam, S., Gandhi, T.K., Panigrahi, B.K., 2020. An improved air-light estimation scheme for single haze images using color constancy prior. IEEE Signal Process. Lett. 27, 1695–1699. <http://dx.doi.org/10.1109/LSP.2020.3025462>.

- Gautam, S., Gandhi, T.K., Panigrahi, B.K., 2021. A model-based dehazing scheme for unmanned aerial vehicle system using radiance boundary constraint and graph model. *J. Vis. Commun. Image Represent.* 74, 102993. <http://dx.doi.org/10.1016/j.jvcir.2020.102993>, URL: <https://www.sciencedirect.com/science/article/pii/S1047320320302108>.
- Gibson, K.B., Vo, D.T., Nguyen, T.Q., 2012. An investigation of dehazing effects on image and video coding. *IEEE Trans. Image Process.* 21 (2), 662–673. <http://dx.doi.org/10.1109/TIP.2011.2166968>.
- Golts, A., Freedman, D., Elad, M., 2020. Unsupervised single image dehazing using dark channel prior loss. *IEEE Trans. Image Process.* 29, 2692–2701.
- Gonzalez, R.C., Woods, R.E., 1992. *Digital Image Processing*, second ed. Addison-Wesley Longman Publishing Co., Inc., Boston, MA, USA.
- Goodfellow, I., Pouget-Abadie, J., Mirza, M., Xu, B., Warde-Farley, D., Ozair, S., Courville, A., Bengio, Y., 2014. Generative adversarial nets. In: Ghahramani, Z., Welling, M., Cortes, C., Lawrence, N.D., Weinberger, K.Q. (Eds.), *Advances in Neural Information Processing Systems 27*. Curran Associates, Inc., pp. 2672–2680, URL: <http://papers.nips.cc/paper/5423-generative-adversarial-nets.pdf>.
- Hautière, N., Tarel, J.-P., Aubert, D., Dumont, É., 2011. Blind contrast enhancement assessment by gradient ratioing at visible edges. *Image Anal. Stereol.* 27 (2), 87–95. <http://dx.doi.org/10.5566/ias.v27.p87-95>, URL: <https://www.ias-iss.org/ojs/IAS/article/view/834>.
- He, K., Sun, J., 2015. Fast guided filter. <http://dx.doi.org/10.48550/ARXIV.1505.00996>, URL: <https://arxiv.org/abs/1505.00996>.
- He, K., Sun, J., Tang, X., 2011. Single image haze removal using dark channel prior. *IEEE Trans. Pattern Anal. Mach. Intell.* 33 (12), 2341–2353. <http://dx.doi.org/10.1109/TPAMI.2010.168>.
- He, J., Xing, F.Z., Yang, R., Zhang, C., 2019. Fast single image dehazing via multilevel wavelet transform based optimization. *CoRR abs/1904.08573*. URL: <http://arxiv.org/abs/1904.08573>, arXiv:1904.08573.
- Jiang, Y., Sun, C., Zhao, Y., Yang, L., 2017. Image dehazing using adaptive bi-channel priors on superpixels. *Comput. Vis. Image Underst.* 165, 17–32. <http://dx.doi.org/10.1016/j.cvi.2017.10.014>, URL: <http://www.sciencedirect.com/science/article/pii/S1077314217301777>.
- Ju, M., Ding, C., Guo, Y.J., Zhang, D., 2019. Remote sensing image haze removal using gamma-correction-based dehazing model. *IEEE Access* 7, 5250–5261. <http://dx.doi.org/10.1109/ACCESS.2018.2889766>.
- Ju, M., Ding, C., Guo, Y.J., Zhang, D., 2020. IDGCP: Image dehazing based on gamma correction prior. *IEEE Trans. Image Process.* 29, 3104–3118. <http://dx.doi.org/10.1109/TIP.2019.2957852>.
- Ju, M., Ding, C., Ren, W., Yang, Y., Zhang, D., Guo, Y.J., 2021. IDE: Image dehazing and exposure using an enhanced atmospheric scattering model. *IEEE Trans. Image Process.* 30, 2180–2192. <http://dx.doi.org/10.1109/TIP.2021.3050643>.
- Kapoor, R., Gupta, R., Son, L.H., Kumar, R., Jha, S., 2019. Fog removal in images using improved dark channel prior and contrast limited adaptive histogram equalization. *Multimedia Tools Appl.* 78 (16), 23281–23307. <http://dx.doi.org/10.1007/s11042-019-7574-8>.
- Kar, A., Dhara, S.K., Sen, D., Biswas, P.K., 2020. Transmission map and atmospheric light guided iterative updaters network for single image dehazing. [arXiv:2008.01701](http://arxiv.org/abs/2008.01701).
- Kim, J.-H., Jang, W.-D., Sim, J.-Y., Kim, C.-S., 2013. Optimized contrast enhancement for real-time image and video dehazing. *J. Vis. Commun. Image Represent.* 24 (3), 410–425. <http://dx.doi.org/10.1016/j.jvcir.2013.02.004>, URL: <http://www.sciencedirect.com/science/article/pii/S1047320313000242>.
- Kim, S.E., Park, T.H., Eom, I.K., 2020. Fast single image dehazing using saturation based transmission map estimation. *IEEE Trans. Image Process.* 29, 1985–1998. <http://dx.doi.org/10.1109/TIP.2019.2948279>.
- Li, H., Li, J., Zhao, D., Xu, L., 2021a. DehazeFlow: Multi-scale conditional flow network for single image dehazing. In: *Proceedings of the 29th ACM International Conference on Multimedia*. Association for Computing Machinery, New York, NY, USA, pp. 2577–2585, URL: <https://doi.org/10.1145/3474085.3475432>.
- Li, Y., Liu, Y., Yan, Q., Zhang, K., 2021b. Deep dehazing network with latent ensembling architecture and adversarial learning. *IEEE Trans. Image Process.* 30, 1354–1368. <http://dx.doi.org/10.1109/TIP.2020.3044208>.
- Li, R., Pan, J., Li, Z., Tang, J., 2018. Single image dehazing via conditional generative adversarial network. In: *2018 IEEE/CVF Conference on Computer Vision and Pattern Recognition*. pp. 8202–8211. <http://dx.doi.org/10.1109/CVPR.2018.00856>.
- Li, B., Peng, X., Wang, Z., Xu, J., Feng, D., 2017a. AOD-Net: All-in-one dehazing network. In: *2017 IEEE International Conference on Computer Vision*. ICCV pp. 4780–4788. <http://dx.doi.org/10.1109/ICCV.2017.511>.
- Li, B., Peng, X., Wang, Z., Xu, J., Feng, D., 2017b. AOD-Net: All-in-one dehazing network. In: *The IEEE International Conference on Computer Vision*. ICCV.
- Li, B., Ren, W., Fu, D., Tao, D., Feng, D., Zeng, W., Wang, Z., 2019. Benchmarking single-image dehazing and beyond. *IEEE Trans. Image Process.* 28 (1), 492–505.
- Li, Y., You, S., Brown, M.S., Tan, R.T., 2017c. Haze visibility enhancement: A survey and quantitative benchmarking. *Comput. Vis. Underst.* 165, 1–16. <http://dx.doi.org/10.1016/j.cvi.2017.09.003>, URL: <https://www.sciencedirect.com/science/article/pii/S1077314217301595>.
- Li, Y., Al-Shehari, H., Zhang, H., 2022. Attention mechanism enhancement algorithm based on cycle consistent generative adversarial networks for single image dehazing. *J. Vis. Commun. Image Represent.* 83, 103434. <http://dx.doi.org/10.1016/j.jvcir.2021.103434>, URL: <https://www.sciencedirect.com/science/article/pii/S1047320321002935>.
- Liu, Z., Xiao, B., Alrabeiah, M., Wang, K., Chen, J., 2019. Single image dehazing with a generic model-agnostic convolutional neural network. *IEEE Signal Process. Lett.* 26 (6), 833–837. <http://dx.doi.org/10.1109/LSP.2019.2910403>.
- Liu, X., Zhang, H., ming Cheung, Y., You, X., Tang, Y.Y., 2017. Efficient single image dehazing and denoising: An efficient multi-scale correlated wavelet approach. *Comput. Vis. Image Underst.* 162, 23–33. <http://dx.doi.org/10.1016/j.cvi.2017.08.002>, URL: <http://www.sciencedirect.com/science/article/pii/S1077314217301431>.
- Lu, Z., Long, B., Yang, S., 2020. Saturation based iterative approach for single image dehazing. *IEEE Signal Process. Lett.* 27, 665–669. <http://dx.doi.org/10.1109/LSP.2020.2985570>.
- Meng, G., Wang, Y., Duan, J., Xiang, S., Pan, C., 2013. Efficient image dehazing with boundary constraint and contextual regularization. In: *2013 IEEE International Conference on Computer Vision*. pp. 617–624. <http://dx.doi.org/10.1109/ICCV.2013.82>.
- Narasimhan, S.G., Nayar, S.K., 2002. Vision and the atmosphere. *Int. J. Comput. Vis.* 48 (3), 233–254. <http://dx.doi.org/10.1023/A:1016328200723>.
- Ponomarenko, N.N., Silvestri, F., Egiazarian, K.O., Carli, M., Astola, J., Lukin, V.V., 2007. On between-coefficient contrast masking of DCT basis functions. In: *Proceedings of the Second International Workshop on Video Processing and Quality Metrics*, Vol. 4.
- Qu, Y., Chen, Y., Huang, J., Xie, Y., 2019. Enhanced pix2pix dehazing network. In: *Proceedings of the IEEE/CVF Conference on Computer Vision and Pattern Recognition*. CVPR.
- Ren, W., Liu, S., Zhang, H., Pan, J., Cao, X., Yang, M.-H., 2016. Single image dehazing via multi-scale convolutional neural networks. In: Leibe, B., Matas, J., Sebe, N., Welling, M. (Eds.), *Computer Vision – ECCV 2016*. Springer International Publishing, Cham, pp. 154–169.
- Ren, W., Ma, L., Zhang, J., Pan, J., Cao, X., Liu, W., Yang, M.-H., 2018. Gated fusion network for single image dehazing. In: *IEEE Conference on Computer Vision and Pattern Recognition*.
- Singh, D., Kumar, V., 2018. Dehazing of remote sensing images using fourth-order partial differential equations based trilateral filter. *IET Comput. Vis.* 12 (2), 208–219. <http://dx.doi.org/10.1049/iet-cvi.2017.0044>.
- Sun, Z., Zhang, Y., Bao, F., Shao, K., Liu, X., Zhang, C., 2021. ICycleGAN: Single image dehazing based on iterative dehazing model and CycleGAN. *Comput. Vis. Image Underst.* 203, 103133. <http://dx.doi.org/10.1016/j.cvi.2020.103133>, URL: <https://www.sciencedirect.com/science/article/pii/S1077314220301521>.
- Tang, K., Yang, J., Wang, J., 2014. Investigating haze-relevant features in a learning framework for image dehazing. In: *2014 IEEE Conference on Computer Vision and Pattern Recognition*. pp. 2995–3002. <http://dx.doi.org/10.1109/CVPR.2014.383>.
- Tarel, J., Hautiere, N., Caraffa, L., Cord, A., Halmaoui, H., Gruyer, D., 2012. Vision enhancement in homogeneous and heterogeneous fog. *IEEE Intell. Transp. Syst. Mag.* 4 (2), 6–20. <http://dx.doi.org/10.1109/MITS.2012.2189969>.
- Tripathi, A.K., Mukhopadhyay, S., 2012. Single image fog removal using anisotropic diffusion. *IET Image Process.* 6 (7), 966–975. <http://dx.doi.org/10.1049/iet-ipr.2011.0472>.
- Wang, A., Wang, W., Liu, J., Gu, N., 2019. AIPNet: Image-to-image single image dehazing with atmospheric illumination prior. *IEEE Trans. Image Process.* 28 (1), 381–393. <http://dx.doi.org/10.1109/TIP.2018.2868567>.
- Wu, H., Qu, Y., Lin, S., Zhou, J., Qiao, R., Zhang, Z., Xie, Y., Ma, L., 2021. Contrastive learning for compact single image dehazing. In: *2021 IEEE/CVF Conference on Computer Vision and Pattern Recognition*. CVPR, pp. 10546–10555. <http://dx.doi.org/10.1109/CVPR46437.2021.01041>.
- Wu, Q., Zhang, J., Ren, W., Zuo, W., Cao, X., 2020. Accurate transmission estimation for removing haze and noise from a single image. *IEEE Trans. Image Process.* 29, 2583–2597.
- Yang, D., Sun, J., 2018. Proximal dehaze-net: A prior learning-based deep network for single image dehazing. In: *ECCV*.
- Zhang, H., Patel, V.M., 2018. Densely connected pyramid dehazing network. In: *2018 IEEE/CVF Conference on Computer Vision and Pattern Recognition*. pp. 3194–3203. <http://dx.doi.org/10.1109/CVPR.2018.00337>.
- Zhang, H., Sindagi, V., Patel, V.M., 2020. Joint transmission map estimation and dehazing using deep networks. *IEEE Trans. Circuits Syst. Video Technol.* 30 (7), 1975–1986. <http://dx.doi.org/10.1109/TCSVT.2019.2912145>.

- Zhang, J., Tao, D., 2020. FAMED-Net: A fast and accurate multi-scale end-to-end dehazing network. *IEEE Trans. Image Process.* 29, 72–84. <http://dx.doi.org/10.1109/TIP.2019.2922837>.
- Zhang, L., Zhang, L., Mou, X., Zhang, D., 2011. FSIM: A feature similarity index for image quality assessment. *IEEE Trans. Image Process.* 20 (8), 2378–2386. <http://dx.doi.org/10.1109/TIP.2011.2109730>.
- Zhao, X., Ding, W., Liu, C., Li, H., 2018. Haze removal for unmanned aerial vehicle aerial video based on spatial-temporal coherence optimisation. *IET Image Process.* 12 (1), 88–97. <http://dx.doi.org/10.1049/iet-ipr.2017.0060>.
- Zhao, D., Xu, L., Yan, Y., Chen, J., Duan, L.-Y., 2019a. Multi-scale optimal fusion model for single image dehazing. *Signal Process., Image Commun.* 74, 253–265. <http://dx.doi.org/10.1016/j.image.2019.02.004>, URL: <http://www.sciencedirect.com/science/article/pii/S0923596518308804>.
- Zhao, J., Zhang, J., Li, Z., Hwang, J.-N., Gao, Y., Fang, Z., Jiang, X., Huang, B., 2019b. DD-CycleGAN: Unpaired image dehazing via double-discriminator cycle-consistent generative adversarial network. *Eng. Appl. Artif. Intell.* 82, 263–271. <http://dx.doi.org/10.1016/j.engappai.2019.04.003>, URL: <http://www.sciencedirect.com/science/article/pii/S0952197619300806>.
- Zhao, S., Zhang, L., Shen, Y., Zhou, Y., 2021. RefineDNet: A weakly supervised refinement framework for single image dehazing. *IEEE Trans. Image Process.* 30, 3391–3404. <http://dx.doi.org/10.1109/TIP.2021.3060873>.
- Zhu, Q., Mai, J., Shao, L., 2015. A fast single image haze removal algorithm using color attenuation prior. *IEEE Trans. Image Process.* 24 (11), 3522–3533. <http://dx.doi.org/10.1109/TIP.2015.2446191>.